

Conductivity of Two-dimensional Dirac Electrons Close to Merging in Organic Conductor α -STF₂I₃ at Ambient Pressure

Yoshikazu Suzumura^{1*} and Toshio Naito^{2,3,4†}

¹*Department of Physics, Nagoya University, Nagoya 464-8602, Japan*

²*Graduate School of Science and Engineering, Ehime University, Matsuyama 790-8577, Japan*

³*Research Unit for Development of Organic Superconductors, Ehime University, Matsuyama 790-8577, Japan*

⁴*Geodynamics Research Center (GRC), Ehime University, Matsuyama 790-8577, Japan*

(Received December 27, 2021; accepted March 16, 2022; published online April 27, 2022)

The electric conductivity of Dirac electrons in the organic conductor α -STF₂I₃ (STF = bis(ethylenedithio)diselenadithiafulvalene), which has an isostructure of α -(BEDT-TTF)₂I₃, has been theoretically studied using a two-dimensional tight-binding model in the presence of both impurity and electron–phonon (e–p) scatterings. In contrast to α -(BEDT-TTF)₂I₃, which has a Dirac cone with almost isotropic velocity, α -STF₂I₃ provides a large anisotropy owing to a Dirac point that is close to merging. As a result, σ_x becomes much larger than σ_y , where σ_y and σ_x are diagonal conductivities parallel and perpendicular to a stacking axis of molecules, respectively. With increasing temperature (T), σ_x takes a broad maximum because of e–p scattering and σ_y remains almost constant. The ratio σ_x/σ_y is analyzed in terms of the band structure. Such an exotic conductivity of α -STF₂I₃ is compared with that of an experiment showing a good correspondence. Finally, σ_x/σ_y values of α -ET₂I₃ and α -BETS₂I₃ are shown to demonstrate the dissimilarity with α -STF₂I₃.

1. Introduction

Since the discovery of two-dimensional massless Dirac fermions,¹⁾ extensive studies have been explored in relevant materials. In particular, Dirac electrons have been found in the organic conductor^{2,3)} α -(BEDT-TTF)₂I₃ (BEDT-TTF=bis(ethylenedithio)tetrathiafulvalene) under uniaxial pressures. Using a tight-binding (TB) model, where transfer energies are estimated by the extended Hückel method,^{4,5)} we found that the density of states (DOS) vanishes linearly at the Fermi energy,⁶⁾ and the two-dimensional Dirac cone gives a zero-gap state (ZGS).²⁾ Such a Dirac cone was verified by first-principles DFT calculation,⁷⁾ which has been utilized for studying the electronic properties of α -(BEDT-TTF)₂I₃ under hydrostatic pressures.⁸⁾

There are several salts with an isostructure in organic conductors,^{9,10)} α -D₂I₃ (D = ET, STF, and BETS), where ET = BEDT-TTF; STF = bis(ethylenedithio)diselenadithiafulvalene, and BETS = bis(ethylenedithio)tetraselenadithiafulvalene. These salts show an energy band with a Dirac cone^{2,11–15)} and a nearly constant resistivity at high temperatures.^{9,10,16–20)}

The conductivity (or resistivity) of Dirac electrons has been studied theoretically using a two-band model with the conduction and valence bands. For a zero-doping, the static conductivity in the limit of absolute zero temperature remains finite with a universal value owing to a quantum effect.²¹⁾ The tilting of the Dirac cone provides the anisotropic conductivity, which results in the deviation of the current from the applied electric field.²²⁾ At finite temperatures (T), the conductivity remains un-

changed for $T < \Gamma$, where Γ corresponds to the inverse of the lifetime determined from the impurity scattering. On the other hand, for $\Gamma \ll T$ the conductivity increases in proportion to T .²³⁾ Since $\Gamma \sim 0.0003$ eV for organic conductors,³⁾ a monotonic increase in the conductivity at high temperature ($T > 0.0005$ eV) is theoretically expected. However, the measurement of the resistivity on the organic conductor shows an almost constant behavior at high temperatures. As a possible mechanism for such an exotic phenomenon, acoustic phonon scatterings have been proposed using the two-band model of the Dirac cone without tilting.²⁴⁾ Thus, it is necessary to clarify if such a mechanism reasonably explains the T dependence of the conductivity of the actual organic conductor with the Dirac cone. In fact, the T dependence of the conductivity in the presence of electron–phonon (e–p) scattering has been calculated for α -ET₂I₃²⁵⁾ and α -BETS₂I₃.²⁶⁾ As common features, they exhibit a small anisotropy at low temperatures and a nearly constant behavior at high temperatures. However, it is unclear if a similar behavior can be expected for α -STF₂I₃, which contains disordered Se and S atoms with equal probabilities (50%:50%) for inner four chalcogen atoms [Fig. 1(a)]. Note that many of the STF salts exhibit electrical properties that indicate intermediate behavior between the isostructural ET and BETS salts, as if the solids do not contain any disorder but consist of a symmetrical donor containing imaginary atoms between selenium and sulfur at the inner chalcogen atoms.^{10,27–29)}

In this paper, we examine the conductivity of α -STF₂I₃ using a TB model with transfer energies, which are improved from a previous work.¹⁵⁾ The model³⁰⁾ provides an electronic state with Dirac points close to merging, which has been theoretically shown in terms of the

*E-mail: suzumura@s.phys.nagoya-u.ac.jp

†E-mail: tnaio@ehime-u.ac.jp

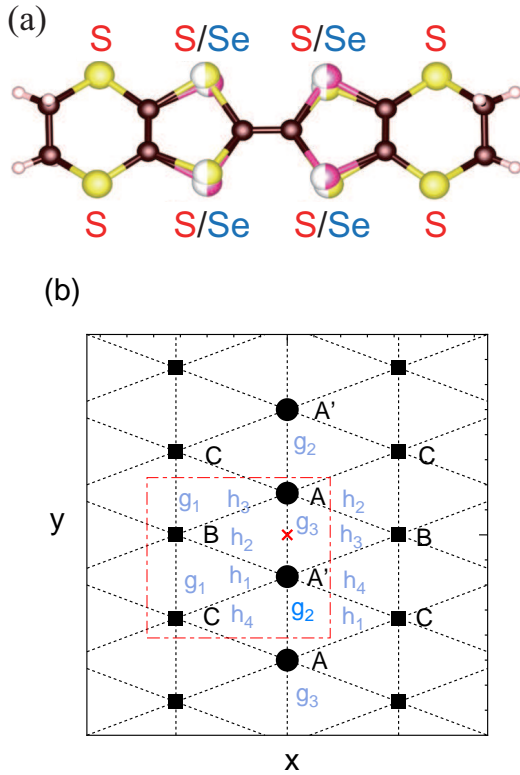


Fig. 1. (Color online) (a) Molecular structure of STF, where STF = bis(ethylenedithio)diselenadithiafulvalene. The small and open circles designate carbon and hydrogen atoms, respectively. For sulfur (S) and selenium (Se), S/Se denotes that the site occupancy is given by S:Se = 50%:50%.¹⁵⁾ (b) TB model of α -D₂I₃ (symbols) on the x - y (crystallographic b - a) plane. A unit cell (dot-dashed line), which forms a square lattice, consists of four molecules A, A', B, and C. The cross denotes an inversion center located in the middle of A and A'. The stacking direction corresponds to the y -axis (i.e., a -axis). Transfer energies between the nearest neighbor (NN) sites are shown by g_1, \dots, h_4 .

effective Hamiltonian.^{31–33)} This paper is organized as follows. In Sect. 2, we briefly mention the difference in the estimation of transfer energies between our previous model¹⁵⁾ and the present one.³⁰⁾ Our Hamiltonian consists of a TB model, impurity scattering, and e-p interaction with a reasonable coupling constant (λ) taken for an organic conductor. In Sect. 3, first, Dirac electrons are examined using the energy band and density of states. Next, the T dependence of anisotropic conductivity, σ_x (σ_y) being perpendicular (parallel) to the stacking axis, is calculated both in the absence and presence of e-p interaction. The ratio of σ_x/σ_y is examined with several choices of λ . In Sect. 4, our calculation is compared with experimental results,^{34,35)} by choosing a reasonable magnitude of λ . Section 5 is devoted to a summary and comparison of the σ_x/σ_y of α -STF₂I₃ with those of α -ET₂I₃ and α -BETS₂I₃.

2. Model and Formulation

2.1 Transfer energies of α -STF₂I₃

Figure 1(a) shows the molecular structure and Fig. 1(b) shows the model describing crystal structures. The choice in the assignment of S or Se atoms for the in-

ner chalcogen atoms in Fig. 1(a) produces randomness, which is given by the atom S/Se or Se/S around the central C=C bond, i.e., atoms on the left-hand side are given by S (pattern 1) or Se (pattern 2). The probabilities of these two patterns are exactly equal, forming a disordered crystal. In a previous model,¹⁵⁾ the transfer integral between nearest neighbor sites in Fig. 1(b) was calculated assuming statistically averaged structures between all the possible molecular arrangements coming from patterns 1 and 2. The present model was obtained by averaging the transfer energies of two extreme cases, which were deduced from the following consideration.³⁰⁾ Note that single-crystal X-ray structural analyses revealed that all the inner four chalcogen atoms in Fig. 1(a) possess equal electron densities;^{28,35)} thus, all the electron densities are obtained by averaging all the inner chalcogen atoms, suggesting a delocalized wave function. Instead of the previous localized wave functions of patterns 1 and 2, our new method provides a delocalized wave function, which is given by a linear combination of the patterns 1 and 2.³⁰⁾ Such a delocalized wave function originates in a quantum interference between the two patterns. Expressing the wave function in terms of atomic orbitals and discarding the off-diagonal elements between S and Se, we obtain the following transfer energies. By rewriting the linear combination in terms of orbitals consisting of only S or Se, they are given by³⁰⁾ $g_1 = 0.0535$, $g_2 = 0.132$, $g_3 = 0.0475$, $h_1 = -0.0295$, $h_2 = 0.295$, $h_3 = 0.1415$, and $h_4 = 0.009$.

2.2 Hamiltonian

We consider a two-dimensional Dirac electron system given by

$$H_{\text{total}} = H_0 + H_p + H_{e-p} + H_{\text{imp}}. \quad (1)$$

The spin is discarded. H_0 describes a TB model of α -STF₂I₃ consisting of four molecules per unit cell (Fig. 1(b)). H_p and H_{e-p} denote an acoustic phonon and an e-p interaction, respectively. H_{imp} is the impurity potential. The terms $H_0 + H_p + H_{e-p}$ provide the Fröhlich Hamiltonian³⁶⁾ applied to the present Dirac electron system. The unit of energy is eV.

The TB Hamiltonian is expressed as

$$\begin{aligned} H_0 &= \sum_{i,j=1}^N \sum_{\alpha,\beta=1}^4 t_{i,j;\alpha,\beta} a_{i,\alpha}^\dagger a_{j,\beta} \\ &= \sum_{\mathbf{k}} \sum_{\alpha,\beta=1}^4 t_{\alpha,\beta}(\mathbf{k}) a_{\alpha}^\dagger(\mathbf{k}) a_{\beta}(\mathbf{k}), \end{aligned} \quad (2)$$

where $a_{i,\alpha}^\dagger$ denotes a creation operator of the electron with molecule α [$= A, A', B, \text{ and } C$] at the i -th site. $a_j = 1/N^{1/2} \sum_{\mathbf{k}} a_{\alpha}(\mathbf{k}) \exp[i\mathbf{k} \cdot \mathbf{r}_j]$ with $\mathbf{k} = (k_x, k_y)$, and N denotes the total number of lattices. The lattice constant is taken as unity. The transfer energies $t_{i,j;\alpha,\beta}$ are expressed in terms of g_1, \dots, h_4 . The matrix elements $t_{\alpha,\beta}(\mathbf{k})$ ($\alpha, \beta = 1, \dots, 4$) in Eq. (2) are given by $t_{12}(\mathbf{k}) = g_3 + g_2Y$, $t_{13}(\mathbf{k}) = h_3 + h_2X$, $t_{14}(\mathbf{k}) = h_4Y + h_1XY$, $t_{23}(\mathbf{k}) = h_2 + h_3X$, $t_{24}(\mathbf{k}) = h_1 + h_4X$, $t_{34}(\mathbf{k}) = g_1 + g_1Y$, and $t_{ij}(\mathbf{k}) = t_{ji}^*(\mathbf{k})$ with $t_{ii}(\mathbf{k}) = 0$, where $X = \exp[ik_x]$

and $Y = \exp[ik_y]$.

Equation (2) is diagonalized as

$$\sum_{\beta=1}^4 t_{\alpha,\beta}(\mathbf{k}) d_{\beta\gamma}(\mathbf{k}) = E_\gamma(\mathbf{k}) d_{\alpha\gamma}(\mathbf{k}), \quad (3)$$

where $E_1(\mathbf{k}) > E_2(\mathbf{k}) > E_3(\mathbf{k}) > E_4(\mathbf{k})$. The Dirac point (\mathbf{k}_D) is calculated from

$$E_1(\mathbf{k}_D) = E_2(\mathbf{k}_D) = \epsilon_D. \quad (4)$$

The ZGS is obtained when ϵ_D becomes equal to the chemical potential at $T=0$.

The chemical potential μ is determined under the three-quarter-filled condition, which is given by

$$\begin{aligned} \frac{1}{N} \sum_{\mathbf{k}} \sum_{\gamma=1}^4 f(E_\gamma(\mathbf{k}) - \mu) \\ = \int_{-\infty}^{\infty} d\omega D(\omega) f(\omega - \mu) = 3, \end{aligned} \quad (5)$$

where $f(\epsilon) = 1/(\exp[\epsilon/T] + 1)$ with T being temperature in eV and $k_B = 1$ and

$$D(\omega) = \frac{1}{N} \sum_{\mathbf{k}} \sum_{\gamma} \delta(\omega - E_\gamma(\mathbf{k})). \quad (6)$$

$D(\omega)$ denotes the density of states (DOS) per unit cell, which satisfies $\int d\omega D(\omega) = 4$.

In Eq. (1), the third term denotes the harmonic phonon given by $H_p = \sum_{\mathbf{q}} \omega_{\mathbf{q}} b_{\mathbf{q}}^\dagger b_{\mathbf{q}}$ with $\omega_{\mathbf{q}} = v_s |\mathbf{q}|$ and $\hbar = 1$, whereas the fourth term is the e-p interaction expressed as³⁶⁾

$$H_{e-p} = \sum_{\mathbf{k}, \gamma} \sum_{\mathbf{q}} \alpha_{\mathbf{q}} c_\gamma(\mathbf{k} + \mathbf{q})^\dagger c_\gamma(\mathbf{k}) \phi_{\mathbf{q}}, \quad (7)$$

with $\phi_{\mathbf{q}} = b_{\mathbf{q}} + b_{-\mathbf{q}}^\dagger$. The e-p scattering is considered within the same band (i.e., intraband) due to the energy conservation with $v \gg v_s$, where $v \simeq 0.05^{(8)}$ denotes the average velocity of the Dirac cone. The last term of Eq. (1), H_{imp} , denotes a normal impurity scattering, which gives a finite conductivity at low temperatures.

2.3 Conductivity

To study the anisotropic conductivity with damping by the impurity and e-p scatterings, we apply the following formula obtained from the linear response theory. Using $d_{\alpha\gamma}$ in Eq. (3), we calculate the conductivity per spin and per site as³⁷⁾

$$\begin{aligned} \sigma_{\nu\nu'}(T) &= \frac{e^2}{\pi \hbar N} \sum_{\mathbf{k}} \sum_{\gamma, \gamma'=1}^4 v_{\gamma\gamma'}^\nu(\mathbf{k})^* v_{\gamma'\gamma}^{\nu'}(\mathbf{k}) \\ &\quad \int_{-\infty}^{\infty} d\epsilon \left(-\frac{\partial f(\epsilon)}{\partial \epsilon} \right) \\ &\quad \times \frac{\Gamma_\gamma}{(\epsilon - \xi_{\gamma, \mathbf{k}})^2 + \Gamma_\gamma^2} \times \frac{\Gamma_{\gamma'}}{(\epsilon - \xi_{\gamma', \mathbf{k}})^2 + \Gamma_{\gamma'}^2}, \end{aligned} \quad (8)$$

$$v_{\gamma\gamma'}^\nu(\mathbf{k}) = \sum_{\alpha, \beta} d_{\alpha\gamma}(\mathbf{k})^* \frac{\partial \tilde{H}_{\alpha\beta}}{\partial k_\nu} d_{\beta\gamma'}(\mathbf{k}). \quad (9)$$

$\xi_{\gamma, \mathbf{k}} = E_\gamma(\mathbf{k}) - \mu$. $\nu = x$ and y . $\hbar = 2\pi\hbar$ and e denote Planck's constant and electric charge, respectively. The quantity Γ_γ denotes the damping of the electron of the γ band given by

$$\Gamma_\gamma = \Gamma + \Gamma_{\text{ph}}^\gamma, \quad (10)$$

where the first term comes from the impurity scattering and the second term corresponding to the phonon scattering is given by²⁴⁾

$$\begin{aligned} \Gamma_{\text{ph}}^\gamma &= \frac{25\lambda}{2\pi v_x v_y} \times T |\xi_{\gamma, \mathbf{k}}| \\ &= C_0 R \times T |\xi_{\gamma, \mathbf{k}}|, \end{aligned} \quad (11a)$$

$$R = \frac{\lambda}{\lambda_0}. \quad (11b)$$

λ is given by $\lambda = |\alpha_{\mathbf{q}}|^2 / \omega_{\mathbf{q}}$ and becomes independent of $|\mathbf{q}|$ for small $|\mathbf{q}|$. v_x (v_y) denotes the velocity of the Dirac cone along the x (y) axis. Since the estimation of λ is complicated for organic conductors, we use an experimentally and theoretically deduced value λ_0 for one-dimensional conductor TCNQ salts, which gives $\lambda_0 N(0) \sim 0.4$.^{38,39)} The quantity $N(0)$ is the density of states given by $2/\pi v_F$. For simplicity, the Fermi velocity v_F is replaced by the average velocity $(v_x v_y)^{1/2} = v$. In the present calculation, we take $\lambda_0 / 2\pi v = 0.1$, which is the same order as that of TCNQ. Thus, we introduce $R = \lambda / \lambda_0$ instead of λ , where $C_0 = 25\lambda_0 / (2\pi v^2) \simeq 50$ (eV)⁻¹ with $v \simeq 0.05$.⁸⁾ Note that $R = 1$ corresponds to $\lambda = \lambda_0$. Compared with Ref. 24, Eq. (11a) is multiplied by 4 owing to the freedom of spin and valley.

3. Conductivity of α -STF₂I₃ close to merging

3.1 Energy band

Dirac electrons close to the merging point are examined by calculating the energy band and DOS using Eq. (2). Figure 2(a) shows the conduction and valence bands, $E_1(\mathbf{k})$ and $E_2(\mathbf{k})$, respectively, measured from the chemical potential (μ) on the plane of the 1st Brillouin zone. Note that the k_x axis of the present choice³⁰⁾ corresponds to $-k_x$ in Ref. 15 due to a different choice of a unit cell. These two bands contact at the Dirac points given by $\pm \mathbf{k}_D = \pm(0.06, 0.21)\pi$, which are close to a merging point given by a time reversal invariant momentum (TRIM) X [= $(\pi, 0)$]. The origin of the energy is taken as the chemical potential of the 3/4-filled band. A pair of Dirac points are close to a merging point, X = $(\pi, 0)$, since $E_1(\mathbf{k}) - E_2(\mathbf{k})$ at $\mathbf{k} = (\pi, 0)$ is much smaller than those at $\mathbf{k} = (0, \pi)$ and (π, π) . Figure 2(b) shows a contour plot of the energy difference $E_1(\mathbf{k}) - E_2(\mathbf{k})$. The Dirac point is found at the darkest region inside the yellow line [$E_1(\mathbf{k}) - E_2(\mathbf{k}) = 0.03$], which is elongated toward the X point. The contour close to the Dirac point shows the ellipse, where the ratio of the major axis to the minor axis is ~ 12 and the major axis is declined clockwise from the k_y axis by an angle $\simeq \cos^{-1}(0.96)$. Note that the Dirac point is close to merging at the X point (TRIM), since the contour shows the ellipse elongated in the direction toward the X point and the velocity in this direction is much reduced.³¹⁻³³⁾ In Fig. 2(c), we

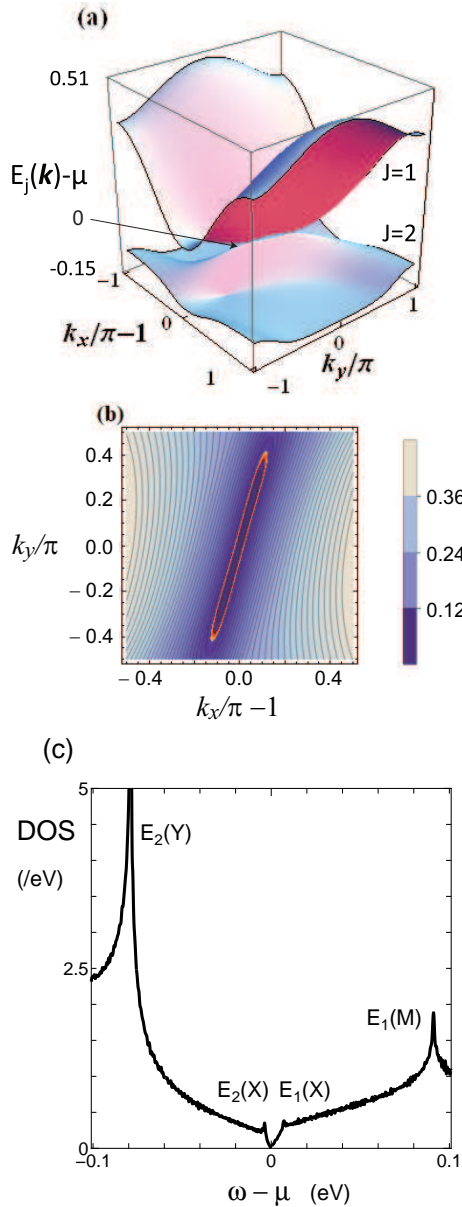


Fig. 2. (Color online) (a) Conduction and valence bands given by $E_1(\mathbf{k})$ (upper band) and $E_2(\mathbf{k})$ (lower band), respectively, on the plane of $(k_x/\pi - 1, k_y/\pi)$,³⁰⁾ measured from the chemical potential $\mu=0.173$. These two bands contact at Dirac points, $\mathbf{k}_D/\pi - (1, 0) = \pm(0.06, 0.21)$ with an energy ϵ_D , which are obtained from $E_1(\mathbf{k}_D) = E_2(\mathbf{k}_D) = \epsilon_D$. (b) Contour plots of $E_1(\mathbf{k}) - E_2(\mathbf{k})$, where a scale is shown by a color bar. The yellow line denotes $E_1(\mathbf{k}) - E_2(\mathbf{k}) = 0.03$, and the inside region represents the main contribution of the present calculation. The Dirac point $\pm\mathbf{k}_D$ exists in the darkest region. (c) DOS as a function of $\omega - \mu$. The large peaks come from the van Hove singularity of the bands at time reversal invariant momenta (TRIMs) $E_1(M)$ and $E_2(Y)$, where $M=(\pi, \pi)$ and $Y=(0, \pi)$. Two peaks around $\omega - \mu = 0$ correspond to the singularity at a TRIM $X=(\pi, 0)$

show DOS corresponding to Fig. 2(a), which is obtained from the conduction (E_1) and valence (E_2) bands. The energy region relevant to the conductivity at low temperatures is within the interval range between two small peaks around $\omega - \mu = 0$. In this region, DOS exhibits a linear dependence because of a Dirac cone. The cusp comes from an anomaly at $E_1(X)$ and $E_2(X)$

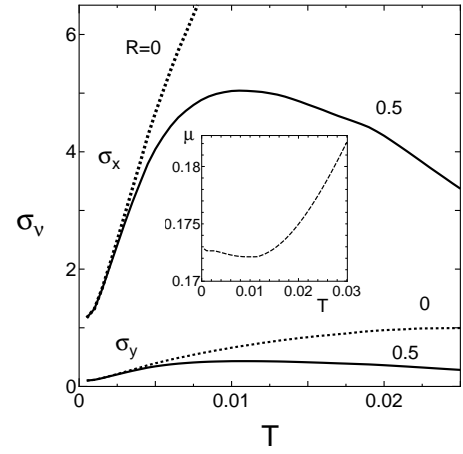


Fig. 3. T dependence of conductivity σ_x and σ_y for $R=0$ (dotted line) and 0.5 (solid line), where $\Gamma = 0.0005$. The inset shows the T dependence of the chemical potential.

3.2 Anisotropic conductivity

We study the anisotropic conductivity by focusing on the diagonal $\sigma_x (= \sigma_{xx})$ and $\sigma_y (= \sigma_{yy})$ (i.e., $\sigma_{xy} < 0$ is not shown) for the comparison with the experimental results. The conductivity calculated from Eq. (8) is normalized by e^2/\hbar . Impurity scattering is taken as $\Gamma = 0.0005$.^{25, 26)}

We examine the conductivity σ_x , which exhibits a dominant contribution to the conductivity. As shown later, the conductivity shows a large anisotropy, i.e., $\sigma_y \ll \sigma_x$, owing to the large anisotropy of the velocity of the Dirac cone.²²⁾ Figure 3 shows the T dependence of the conductivity σ_x for $R=0$ and 0.5 , where $R = 0.5$ is a suitable choice of the e-p coupling constant. The R dependence of σ_x is also examined in Fig. 4. The inset of Fig. 3 denotes the corresponding chemical potential μ , which is calculated from Eq. (5). μ decreases slightly at low temperatures but increases with increasing T due to DOS, where a peak of the valence band (E_2) is larger than that of the conduction band (E_1).

First, we show the T dependence of the conductivity for $R = 0$. The conductivity of a simple Dirac cone with the isotropic and linear dispersion increases linearly with respect to T owing to the linear increase in DOS.²⁴⁾ A monotonic increase in the conductivity is also found for the energy band of the actual organic conductor with anisotropic velocity, although a slight deviation of the linear increase exists.^{25, 26)} Since the conductivity remains constant at low temperatures, the transport of the Dirac electrons is well understood by the impurity scattering. However another scattering is needed to understand the almost constant behavior of σ_x with increasing temperature.²⁴⁾

We next show the effect of e-p scattering on σ_ν ($\nu = x$ and y) using $R = 0.5$. Compared with σ_ν with $R = 0$, the conductivity for $R \neq 0$ at high temperatures is noticeably reduced owing to the increase in $\Gamma_{\text{ph}}^\gamma$ in the denominator of Eq. (8). It turns out that σ_x shows a broad peak but σ_y shows an almost constant behavior. With increasing R , σ_x decreases noticeably at high temperatures ($0.08 < T$),

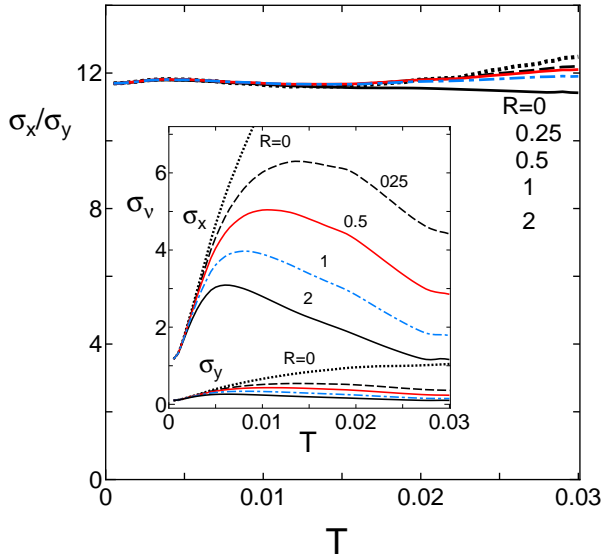


Fig. 4. (Color online) T dependence of σ_x/σ_y for several choices of e-p coupling; $R=0$ (dotted line), 0.25 (dashed line), 0.5 (solid line), 1 (dot-dashed line), and 2 (solid line), where $\Gamma = 0.0005$. The inset shows the T dependence of the corresponding σ_x and σ_y .

whereas the decrease in σ_y is small. Note that such a large reduction in σ_x by R comes from σ_x being much larger than σ_y , which magnifies the behavior of σ_x on a visible scale. The large anisotropy of the conductivity originates from the anisotropy of the velocity v_x being larger than v_y , since $\sigma_x \propto v_x/v_y$ and $\sigma_y \propto v_y/v_x$.²²⁾ As shown in Figs. 2(a) and 2(b), the large anisotropy of the velocity is a characteristic of the Dirac cone close to merging. The difference in σ_ν between $R = 0$ and 0.5 becomes negligibly small for $T < 0.003$, since the e-p interaction becomes ineffective at low temperatures.

The conductivity of $\sigma_\nu(T)$ for $R = 0, 0.25, 0.5, 1,$ and 2 is shown in the inset of Fig. 4. With increasing R ($\propto \lambda$), σ_ν with a fixed T decreases rapidly owing to the increase of the e-p interaction (λ), which appears in the denominator of Eq. (8). Since $\Gamma_{\text{ph}}^\gamma \propto \lambda T$, the peak of σ_x at $T = T_{\text{max}}$ decreases and T_{max} also decreases.

In Fig. 4, the T dependence of σ_x/σ_y is shown to comprehend an anisotropy of the conductivity. At low temperatures, σ_x/σ_y ($\simeq 12$) is almost independent of T and R . At high temperatures ($0.02 < T$), σ_x/σ_y for $R = 0, 0.25, 0.5,$ and 1 (2) increases (decreases) slightly. Such behavior of σ_x/σ_y with respect to T suggests that σ_x/σ_y is determined by v_x/v_y but is almost independent of the scattering by impurities and phonons. Here, we analyze σ_x/σ_y using Fig. 2(b). The contour of $E_1(\mathbf{k}) - E_2(\mathbf{k})$ encircling the Dirac point shows the ellipse with a focus at the Dirac point, and the axis rotated clockwise from the k_y axis with an angle θ . The principal values of the conductivity, σ_+ and σ_- , show $\sigma_+/\sigma_- \simeq (v_+/v_-)^2$. v_+ and v_- are velocities of the Dirac cone corresponding to the minor axis and the major axis of the ellipse, respectively.²²⁾ In terms of θ , σ_+ , and σ_- , the ratio of σ_x to σ_y

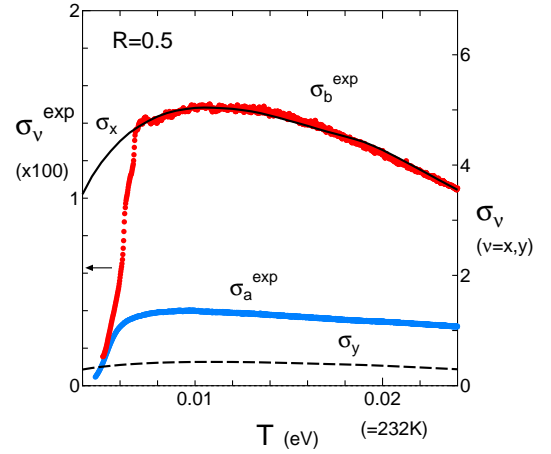


Fig. 5. (Color online) Theoretical results (lines) and those of experiment (symbols),³⁴⁾ where σ_x (σ_y) corresponds to σ_b^{exp} (σ_a^{exp}). σ_x and σ_y are compared with σ_b^{exp} and σ_a^{exp} , respectively.

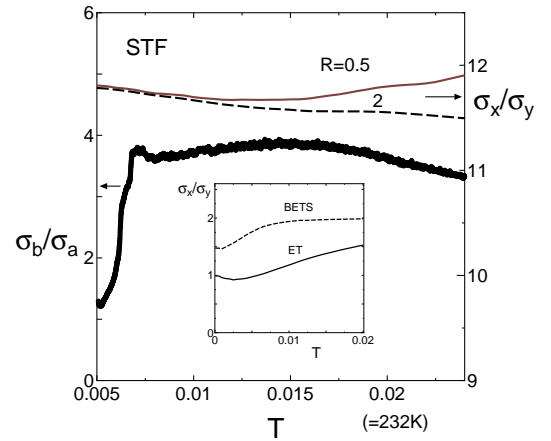


Fig. 6. T dependence of $\sigma_b^{\text{exp}}/\sigma_a^{\text{exp}}$ (symbols) from Ref. 34 and σ_x/σ_y from the present calculation with $R = 0.5$ (solid line) and 2 (dashed line). The inset is discussed in Sect. 5, where σ_x/σ_y values for ET ($R=0.5$) and BETS ($R=1$) were obtained from Refs. 25 and 26, respectively.

is given by

$$\frac{\sigma_x}{\sigma_y} = \frac{(\sigma_+/\sigma_-)^2 + \tan^2 \theta}{(\sigma_+/\sigma_-)^2 \tan^2 \theta + 1}. \quad (12)$$

Substituting $\sigma_+/\sigma_- \simeq 12$ and $\tan \theta \simeq 0.28$ into Eq. (12), we obtain $\sigma_x/\sigma_y \simeq 11.7$, which is almost equal to the numerical value in Fig. 4. Note that σ_x/σ_y is mainly determined by θ for large σ_+/σ_- , i.e., for the case of an extremely elongated ellipse.

4. Comparison with Experiment

Finally, we compare the present theoretical result with that of the experiment,³⁴⁾ where σ_b^{exp} and σ_a^{exp} (symbols) correspond to σ_x and σ_y , respectively. In Fig. 5, σ_x and σ_y are compared with σ_b^{exp} and σ_a^{exp} . The experimental (theoretical) result is shown using the left (right) axis. The e-p coupling constant λ is taken as $R=0.5$ to obtain T_{max} of σ_x equal to that of σ_b^{exp} , where the conductiv-

ity becomes maximum at $T = T_{\max}$. The scale of σ_x is taken such that the maximum σ_b^{exp} becomes equal to the maximum σ_x . A good coincidence between σ_b^{exp} and σ_x is obtained in the region of $0.006 < T < 0.024$. Moreover, a comparison of σ_a^{exp} and σ_y gives $\sigma_a^{\text{exp}} \simeq 4\sigma_y$ for $0.008 < T$, where both show nearly constant behaviors. The rapid decrease in both σ_b^{exp} and σ_a^{exp} for $T \simeq 0.006$ suggests the reduction of the Fermi surface. In fact, the T dependence of the resistivity of α -STF₂I₃ shows a behavior between those of α -ET₂I₃ and α -BETS₂I₃,^{10,28} where the former becomes the insulating state due to charge ordering³) and the latter remains in a metallic state.^{13,14}) Thus, the reduction of the conductivity at low temperature may be ascribed to the charge fluctuation. Namely, the comparison of the present TB model with the experiment may be justified for $0.006 < T$.

In Fig. 6, the T dependence of σ_x/σ_y ($R=0.5$) is compared with that of $\sigma_b^{\text{exp}}/\sigma_a^{\text{exp}}$. The temperature variations of σ_x/σ_y for $0.005 < T$ and $\sigma_b^{\text{exp}}/\sigma_a^{\text{exp}}$ for $0.008 < T$ are small. At higher temperatures, σ_x/σ_y shows a slight increase (decrease) for $R = 0.5$ ($R=2$), whereas $\sigma_b^{\text{exp}}/\sigma_a^{\text{exp}}$ decreases. The broad maximum of $\sigma_b^{\text{exp}}/\sigma_a^{\text{exp}}$ around $T \simeq 0.015$ comes from the fact that σ_b^{exp} takes a broad maximum at $T \simeq 0.012$, whereas σ_a^{exp} for $0.01 < T$ decreases linearly and slowly. The almost constant behavior of σ_x/σ_y suggesting the same T dependence is understood from the magnified scale of σ_x and σ_y , which show a common behavior of a broad maximum at $T \simeq 0.01$. However, the linear dependence in σ_a^{exp} is not yet clear and a further consideration beyond Eq. (11a) may be needed.

5. Summary and Discussion

In summary, we examined the T dependence of the conductivity of Dirac electrons in the organic conductor α -STF₂I₃ at ambient pressure. A large anisotropy, which comes from the Dirac point close to merging, gives rise to the characteristics of σ_ν , where σ_x takes a broad maximum owing to e-p scattering with increasing temperature. The ratio of σ_x/σ_y is almost independent of T owing to the large anisotropy of the velocity and the axes of the ellipse rotated from the k_y and k_x directions. We compared the conductivity in the present calculation with that in the experiment. To our best knowledge, this is the first experimental demonstration of the T dependence of the anisotropic conductivity in organic Dirac electrons. The experimental result of α -STF₂I₃ was reasonably explained by the present calculation of the TB model with e-p interaction. It will be interesting to examine the current deviation from the electric field due to $\sigma_{xy} \neq 0$.

Here, we compare the present σ_x/σ_y of α -STF₂I₃ (Fig. 4) with those of other organic conductors, α -(BEDT-TTF)₂I₃ and α -BETS₂I₃, which show band structures with almost isotropic velocities owing to Dirac points being away from TRIM. In the inset of Fig. 6, the T dependences of σ_x/σ_y for α -(BEDT-TTF)₂I₃ and α -BETS₂I₃ are shown, which display the visible increase with increasing T in contrast to σ_x/σ_y of α -STF₂I₃. For ET (under hydroppressures),²⁵) a small anisotropy of the

velocity ($v_x/v_y \simeq 1.2$) shows $\sigma_x/\sigma_y \simeq 1.4$, which is compensated by the tilting of the Dirac cone ($\eta = v_t/V \simeq 0.8$ with v_t and V being the tilting and averaged velocities of the Dirac cone, respectively). As a result, $\sigma_x/\sigma_y \simeq 1$ at low temperatures and increases with increasing T . For BETS,²⁶) the anisotropy of the velocity ($v_x/v_y \simeq 1.4$) is slightly larger and dominates the effect of tilting ($\eta \simeq 0.8$). Therefore, anisotropic conductivity shows $\sigma_x/\sigma_y \simeq 1.4$ at low temperatures and increases to a finite value with increasing T . Note that σ_x/σ_y of α -ET₂I₃ and α -BETS₂I₃ clearly increases with increasing T owing to almost isotropic velocities. Thus, as shown in Eq. (12), the almost T -independent behavior of $\sigma_x/\sigma_y (\gg 1)$ in α -STF₂I₃ is ascribed to the large anisotropy of the velocity ($v_x/v_y \gg 1$), which originates from the Dirac point close to merging.

Acknowledgements

T.N. acknowledges the support by JSPS KAKENHI Grant Number 22H02034.

- 1) K. S. Novoselov, A. K. Geim, S. V. Morozov, D. Jiang, M. I. Katsnelson, I. V. Grigorieva, S. V. Dubonos, and A. A. Firsov, *Nature* **438**, 197 (2005).
- 2) S. Katayama, A. Kobayashi, and Y. Suzumura, *J. Phys. Soc. Jpn.* **75**, 054705 (2006).
- 3) K. Kajita, Y. Nishio, N. Tajima, Y. Suzumura, and A. Kobayashi, *J. Phys. Soc. Jpn.* **83**, 072002 (2014).
- 4) T. Mori, A. Kobayashi, Y. Sasaki, H. Kobayashi, G. Saito, and H. Inokuchi, *Chem. Lett.* **13**, 957 (1984).
- 5) R. Kondo, S. Kagoshima, and J. Harada, *Rev. Sci. Instrum.* **76**, 093902 (2005).
- 6) A. Kobayashi, S. Katayama, K. Noguchi, and Y. Suzumura, *J. Phys. Soc. Jpn.* **73**, 3135 (2004).
- 7) H. Kino and T. Miyazaki, *J. Phys. Soc. Jpn.* **75**, 034704 (2006).
- 8) S. Katayama, A. Kobayashi, and Y. Suzumura, *Eur. Phys. J. B* **67**, 139 (2009).
- 9) M. Inokuchi, H. Tajima, A. Kobayashi, H. Kuroda, R. Kato, T. Naito, and H. Kobayashi, *Synth. Met.* **56**, 2495 (1993).
- 10) M. Inokuchi, H. Tajima, A. Kobayashi, T. Ohta, H. Kuroda, R. Kato, T. Naito, and H. Kobayashi, *Bull. Chem. Soc. Jpn.* **68**, 547 (1995).
- 11) R. Kondo, S. Kagoshima, N. Tajima, and R. Kato, *J. Phys. Soc. Jpn.* **78**, 114714 (2009).
- 12) T. Morinari and Y. Suzumura, *J. Phys. Soc. Jpn.* **83**, 094701 (2014).
- 13) S. Kitou, T. Tsumuraya, H. Sawahata, F. Ishii, K. Hiraki, T. Nakamura, N. Katayama, and H. Sawa, *Phys. Rev. B* **103**, 035135 (2021).
- 14) T. Tsumuraya and Y. Suzumura, *Eur. Phys. J. B* **94**, 17 (2021).
- 15) T. Naito, R. Doi, and Y. Suzumura, *J. Phys. Soc. Jpn.* **89**, 023701 (2020).
- 16) K. Kajita, T. Ojio, H. Fujii, Y. Nishio, H. Kobayashi, A. Kobayashi, and R. Kato, *J. Phys. Soc. Jpn.* **61**, 23 (1992).
- 17) N. Tajima, M. Tamura, Y. Nishio, K. Kajita, and Y. Iye, *J. Phys. Soc. Jpn.* **69**, 543 (2000).
- 18) N. Tajima, A. Ebina-Tajima, M. Tamura, Y. Nishio, and K. Kajita, *J. Phys. Soc. Jpn.* **71**, 1832 (2002).
- 19) N. Tajima, S. Sugawara, M. Tamura, R. Kato, Y. Nishio, and K. Kajita, *Europhys. Lett.* **80**, 47002 (2007).
- 20) D. Liu, K. Ishikawa, R. Takehara, K. Miyagawa, M. Tanuma, and K. Kanoda, *Phys. Rev. Lett.* **116**, 226401 (2016).
- 21) N. H. Shon and T. Ando, *J. Phys. Soc. Jpn.* **67**, 2421 (1998).
- 22) Y. Suzumura, I. Proskurin, and M. Ogata, *J. Phys. Soc. Jpn.* **83**, 023701 (2014).
- 23) N. M. R. Peres, F. Guinea, and A. H. Castro Neto, *Phys. Rev. B* **73**, 125411 (2006).

- 24) Y. Suzumura and M. Ogata, *Phys. Rev. B* **98**, 161205 (2018).
- 25) Y. Suzumura and M. Ogata, *J. Phys. Soc. Jpn.* **90**, 044709 (2021).
- 26) Y. Suzumura and T. Tsumuraya, *J. Phys. Soc. Jpn.* **90**, 124707 (2021).
- 27) T. Naito, A. Miyamoto, H. Kobayashi, R. Kato, and A. Kobayashi, *Chem. Lett.* **21**, 119 (1992).
- 28) T. Naito, Dr. Thesis, Graduate School of Science, The University of Tokyo, Tokyo (1995).
- 29) T. Naito, H. Kobayashi, and A. Kobayashi, *Bull. Chem. Soc. Jpn.* **70**, 107 (1997).
- 30) T. Naito and Y. Suzumura, *Crystals* **12**, 346 (2022).
- 31) G. Montambaux, F. Piechon, J. -N. Fuchs, and M. O. Goerbig, *Eur. Phys. J. B* **72**, 509 (2009).
- 32) G. Montambaux, F. Piechon, J. -N. Fuchs, and M. O. Goerbig, *Phys. Rev. B* **80**, 153412 (2009).
- 33) A. Kobayashi, Y. Suzumura, F. Piechon, and G. Montambaux, *Phys. Rev. B* **84**, 075450 (2011).
- 34) T. Naito and R. Doi, *Crystals* **10**, 270 (2020).
- 35) T. Naito, *Crystals* **11**, 838 (2021).
- 36) H. Fröhlich, *Proc. Phys. Soc. A* **223**, 296 (1954).
- 37) S. Katayama, A. Kobayashi, and Y. Suzumura, *J. Phys. Soc. Jpn.* **75**, 023708 (2006).
- 38) M. J. Rice, L. Pietronero, and P. Brüesch, *Solid State Commun.* **21**, 757 (1977).
- 39) H. Gutfreund, C. Hartzstein, and M. Weger, *Solid State Commun.* **36**, 647 (1980).